Supporting Information:

Triplet State Delocalization in a Conjugated Porphyrin Dimer Probed by Transient Electron Paramagnetic Resonance Techniques

Claudia E. Tait,† Patrik Neuhaus,‡ Harry L. Anderson,‡ Christiane R. Timmel*,†

†Department of Chemistry, Centre for Advanced Electron Spin Resonance, University of Oxford, South Parks Road, Oxford OX1 3QR, United Kingdom.

‡Department of Chemistry, Chemistry Research Laboratory, University of Oxford, 12 Mansfield Road, Oxford OX1 3TA, United Kingdom.

Experimental Methods

Synthesis and sample preparation

The zinc porphyrin monomer (**P1**) and dimer (**P2**) depicted in Figure 1 of the main text were synthesized according to a previously published procedure.[1] The purity of the synthesized compounds was characterized by NMR, UV−vis and analytical GPC. The EPR measurements were performed on 100-200 μM solutions of **P1** or **P2** in 2-methyltetrahydrofuran (MeTHF): pyridine 10:1. The solutions were degassed by several freeze-pump-thaw cycles and frozen in liquid N_2.

Time-resolved EPR

The time-resolved EPR experiments were performed at X-band on a Bruker Elexsys 680 spectrometer equipped with a helium gas-flow cryostat from Oxford instruments. Laser excitation at 532 nm was provided by the second harmonic of an Nd:YAG laser (Surelite Continuum) with a repetition rate of 10 Hz. Light depolarized with an achromatic depolarizer was used unless otherwise stated. TR-EPR experiments were performed by direct detection with the transient recorder without lock-in amplification; the microwave power was 0.2 mW. The laser background signal was removed by 2D baseline-correction determined based on the off-resonance transients. The spectra were integrated over the first 2 μs after the laser flash. Experiments were typically performed at 20 K, but no changes in the spectra were observed at temperatures between about 100 and 5 K.

Magnetophotoselection experiments were performed with polarized light from an Opotek Opolette Opto-parametric Oscillator (OPO) tunable laser (20 Hz repetition rate) at wavelengths corresponding to the region of the Q-bands in the UV−vis spectra.

Pulse EPR

X-band pulse EPR measurements were performed on a Bruker Elexsys 680 spectrometer with a Bruker EN 4118X-MD4 resonator. The Q-band measurements were performed on a Bruker Elexsys 580 spectrometer in the National EPR facility at the University of Manchester. The measurements were performed at 20 K and with laser excitation as previously described. The repetition rate of the pulse experiments was determined by the laser repetition rate of 10 Hz (20 Hz for measurements with the OPO).

^{1}H Mims ENDOR spectra were recorded with the pulse sequence $\frac{\pi}{2}$-τ-$\frac{\pi}{2}$-T-$\frac{\pi}{2}$-τ-echo with mw pulse lengths of $t_{\pi/2}$=24 ns, τ =120, 160, 200 ns and a radiofrequency pulse length of 15 μs; the RF power was adjusted based on a nutation experiment. The ENDOR spectra were recorded at the canonical field positions of the triplet state EPR spectrum; spectra were recorded for three different τ values (120, 160 and 200 ns) and summed to prevent distortions by blind spots.

X-band three-pulse ESEEM experiments were performed with the pulse sequence $\frac{\pi}{2}$-τ-$\frac{\pi}{2}$-T-$\frac{\pi}{2}$-τ-echo with mw pulses of length $t_{\pi/2}$=16 ns and an initial T value of 64 ns with increments dt =8 ns (1024 data points were collected). In the Q-band three-pulse ESEEM experiments the pulse lengths were $t_{\pi/2}$=20 ns and 512 data points were collected. A 4-step phase cycle was used to remove unwanted echoes. The ESEEM traces were recorded for three different τ values (100 ns, 160 ns and 200 ns) and the FT spectra were summed to avoid distortions due to blind spots. The experimental data were processed with a home-written Matlab program, the time traces were baseline corrected with a stretched exponential, apodized with a Hamming window and zero-filled to 2048 data points. The frequency spectrum was calculated using the cross-term averaging procedure implemented in EasySpin.[2-3]

X-band HYSCORE experiments were performed using the pulse sequence $\frac{\pi}{2}$-τ-$\frac{\pi}{2}$-t_1-π-t_2-$\frac{\pi}{2}$-τ-echo with mw pulses of lengths of $t_{\pi/2}$=16 ns, t_π =16 ns and τ =120, 160 and 200 ns, and starting times t_1=t_2=64 ns with increments dt =16 ns (data matrix 256x256). ^{14}N matched HYSCORE experiments were performed with matched pulses instead of the second and last pulse of the standard HYSCORE sequence. The matched pulses were applied at high microwave power and the pulse lengths were optimized for maximum modulation depth in three-pulse ESEEM experiments with varying pulse lengths (optimum length = 24 ns). Q-band HYSCORE was performed with pulse lengths of $t_{\pi/2}$=30 ns, , t_π =30 ns, τ =100 and 212 ns, and starting times t_1 = t_2 =64 ns with increments dt =16 ns (data matrix 256x256). ^{14}N matched HYSCORE was performed at the Z- field position with 74 ns matched pulses and 8 ns increments, τ values of 100 and 160 ns were used. A 4-step phase cycle was used to remove unwanted echoes. The experimental data were processed in Matlab; the time traces were baseline corrected by a 3rd order polynomial, apodized with a Hamming window and

zero-filled to 1024 points in each dimension. A 2D Fourier transform was applied and the absolute-value spectrum was calculated.

Q-band ENDOR was performed using the Davies sequence for the porphyrin monomer and the Mims sequence for the porphyrin dimer at the field positions corresponding to the out-of-plane orientation (1233.2 mT and 1235.0 mT respectively). Davies ENDOR was performed with the π-T-$\frac{\pi}{2}$-τ-π-τ-echo sequence with an 88 ns inversion pulse, a 16 ns − 32 ns detection sequence and a radiofrequency pulse of 40 μs. Mims ENDOR was performed with the pulse sequence $\frac{\pi}{2}$-τ-$\frac{\pi}{2}$-T-$\frac{\pi}{2}$-τ-echo with 20 ns microwave pulses and a 40 μs radiofrequency pulse. Spectra were recorded with τ values of 100, 176, 252 and 328 ns and summed to avoid distortions due to blind spots.

Spectral Analysis

The spin-polarized powder triplet state spectra were simulated using EasySpin's *pepper* routine.[3] The zero-field splitting parameters *D* and *E*, as well as the relative population probabilities at zero-field, were determined by least-square fitting of the experimental transient EPR data. The energy ordering of the triplet sublevels was chosen as $|Z|>|X|>|Y|$.

The relative orientations of the zero-field splitting tensor orientations and the optical transition dipole moments was determined based on the polarization index calculated from the magnetophotoselection data. The polarization ratio is defined as:[4-5]

$$P_i = \frac{I_i^{\parallel} - I_i^{\perp}}{I_i^{\parallel} + I_i^{\perp}} \quad (1)$$

where $I_i^{\parallel/\perp}$ are the intensities of the derivative EPR signal for excitation with light polarized parallel or perpendicular to the magnetic field at the field positions corresponding to the X, Y or Z orientation of the ZFS tensor. The polarization index was calculated for different wavelengths by integration of the low and high field canonical regions of the derivative spectra; standard deviations were estimated by considering different regions for the integration (derivative signal maximum ±0.05 to ±0.40 mT).

The values of the proton hyperfine couplings along the principal axes of the ZFS tensor were determined by Gaussian deconvolution of the ENDOR spectra. The deconvolutions were performed simultaneously for the low and high field canonical positions with the same hyperfine couplings and FWHMs.

The nitrogen hyperfine and nuclear quadrupole parameters were determined through simultaneous least-square fitting of the X- and Q-band three-pulse ESEEM (both time and frequency domain data), Q-band ENDOR and X- and Q-band HYSCORE data with a home-written Matlab routine. The ESEEM and ENDOR data were simulated with EasySpin[3, 6] and the cross peak positions in the HYSCORE spectra were calculated by exact diagonalization of the Hamiltonian in Matlab. The orientations of the hyperfine and nuclear quadrupole tensors were kept fixed at the values obtained from DFT calculations, which are in agreement with previous findings on similar porphyrin systems.[7]

The optimization of the ^{14}N hyperfine and nuclear quadrupole parameters was performed through Marquardt-Newton-Gauss least-square fitting. The fitting routine simultaneously optimized the agreement with the X- and Q-band time and frequency domain three-pulse ESEEM data, the Q-band ENDOR spectrum and the X- and Q-band HYSCORE spectra. The weighting of the different types of datasets used for the fitting was adjusted by normalization of the root-mean-square deviations with respect to the initial simulation parameter set. A larger weighting was used for the ENDOR data and HYSCORE double-quantum cross-peak data (six and five times larger, respectively), as they contain the most precise information on the hyperfine and nuclear quadrupole parameters.

A distribution of hyperfine and nuclear quadrupole parameters was used in the simulations to reproduce the features observed in the experimental ENDOR and HYSCORE data. A Gaussian weighting function centered on the mean value of each of the parameters and with a full width at half maximum of 2.5 MHz was used. Skewed weighting functions did not correctly reproduce the features observed in the experimental data, i.e. a broad peak in the ENDOR spectrum and ridges in the HYSCORE spectra.

The centers and widths of the distributions of the three principal values of the hyperfine tensor and of the nuclear quadrupole parameters *Q* and η were optimized in the fitting routine. The orientations of the hyperfine and nuclear quadrupole tensors with respect to the zero-field splitting tensor were kept fixed at the values obtained from DFT calculations, which are in agreement with previous findings on similar porphyrin systems. [7]

The error on the simulation parameters was evaluated by performing a grid search in the proximity of the optimised values and considering the root-mean-square deviation values as well as assessing the goodness of fit by visual inspection for the simulations with the lowest RMSD values.

Computational methods

DFT geometry optimizations of the triplet excited state structures for the porphyrin monomer and dimer were performed in ORCA[8-9] with the BP86 functional and the SV(P) basis set using the RI approximation with the auxiliary SV/C basis set. The $Si(C_6H_{13})_3$ groups were replaced by hydrogen atoms and the resulting structures were optimized without symmetry constraints. Calculations of the zero-field splitting interaction were performed according to a procedure published by Sinnecker et al.,[10] using the B3LYP functional and the EPRII basis set[11] and calculating the spin-spin contribution to the ZFS using UNO determinants. The results were compared to calculations with the BP86 and BHLYP functional to evaluate the extent of the self-interaction error and no significant difference was found.

Time-dependent DFT calculations were performed on **P1** to determine the nature of the first excited triplet state. The calculations were again performed with the B3LYP, BP86 and BHLYP functional and the def2-TZVP and def2-TZVP/C basis sets[12] with the RI approximation. The calculations were performed with the Tamm-Dancoff approximation (TDA).[13]

The hyperfine and nuclear quadrupole interaction parameters were calculated with the B3LYP functional and the EPRII basis set, purposely developed for the calculation of EPR hyperfine interaction values, for the C, N and H nuclei[11, 14-15] and the 6-31G(d) basis set for Zn.

The effect of a coordinating pyridine molecule on the geometry of the porphyrin ring in **P1** was investigated by performing a relaxed surface scan with different fixed distances between

the zinc ion of the porphyrin and the nitrogen atom of the pyridine molecule. The hyperfine and nuclear quadrupole interaction parameters were calculated for each of the structures.

Conformation of the porphyrin dimer

Previous investigations have shown that different conformations of the porphyrin dimer, characterized by different torsional angles around the butadiyne link, contribute to the absorption spectrum in different wavelength regions, as indicated in Figure S1.[16] The UV−vis spectrum of the planar conformation has been determined by binding of the porphyrin dimer to a rigid template.[16] The barrier to rotation about the butadiyne link in the porphyrin dimer has been estimated to about 0.7 kcal mol^{-1}, allowing free rotation around the central bond at room temperature. The UV−vis spectrum recorded in MeTHF:pyridine at 80 K, however closely resembles the spectrum of the planar dimer bound to the template, confirming that the planar conformation of the dimer is almost exclusively present under these conditions due to planarization of the molecule upon cooling.[17] Temperature-dependent UV−vis studies performed for a range of different conformations have confirmed that the observed spectral change does not appear to be associated with aggregation.[17]

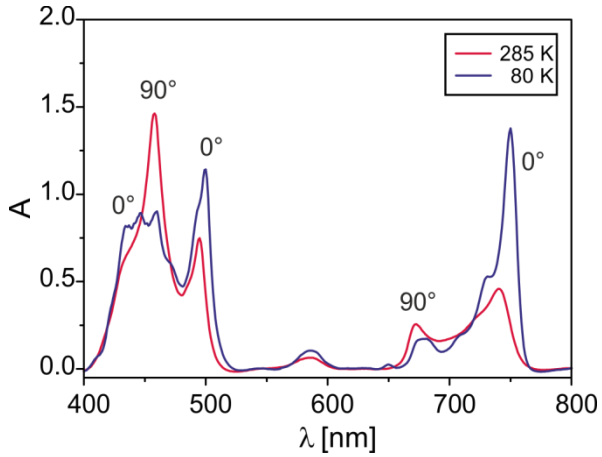

Figure S1. UV−vis absorption spectra of P2 at 285 K and 80 K recorded in MeTHF:pyridine 10:1.[17] The absorption bands in the spectra have been assigned to the planar (0°) and twisted (90°) conformations of the porphyrin dimer according to reference 16.

^{14}N HYSCORE spectra without pyridine

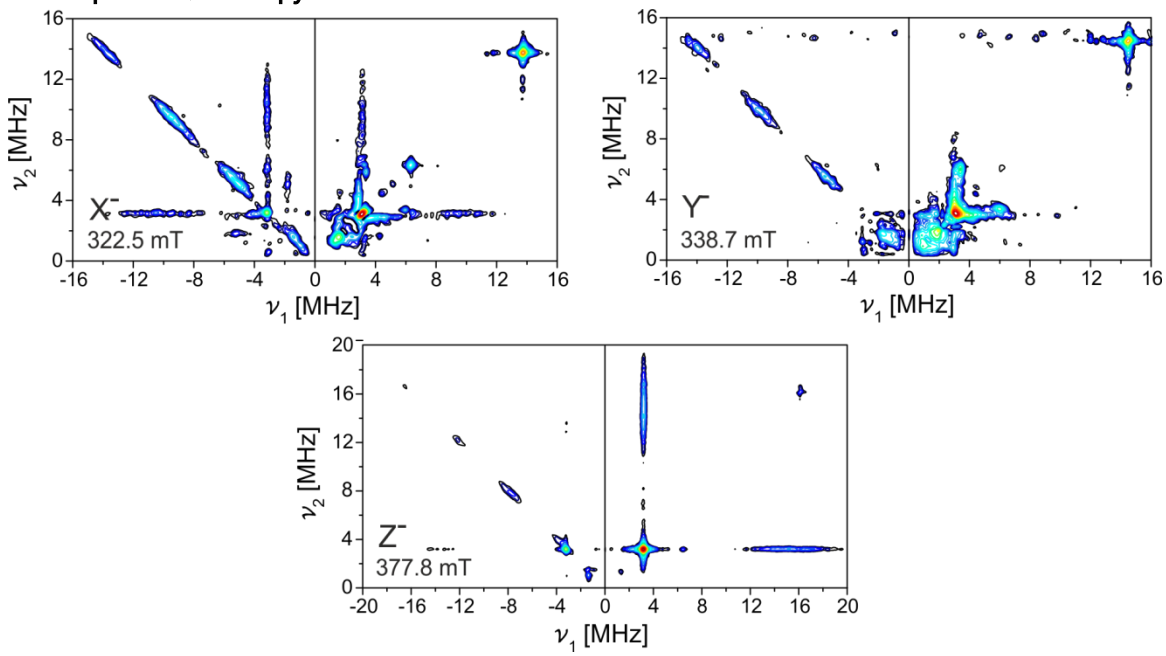

Figure S2. Experimental X-band HYSCORE spectra for the X^-, Y^- and Z^- field positions for **P1** in MeTHF without pyridine recorded at 20 K. The Z^- spectrum was recorded using ^{14}N matched HYSCORE.

Results of DFT calculations

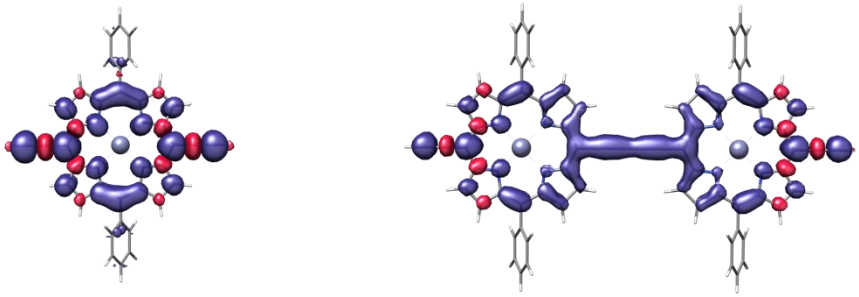

Figure S3. Spin density distributions calculated at B3LYP/EPRII level for the porphyrin monomer (**P1**) and dimer (**P2**) in ORCA.[9]

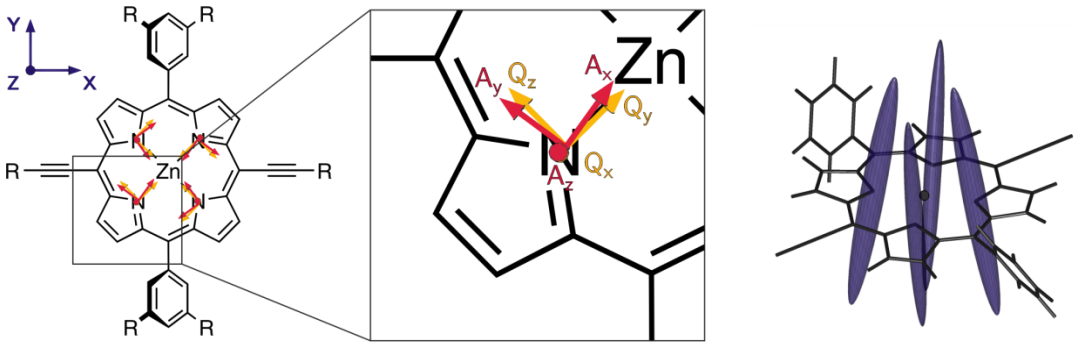

Figure S4. Diagram of the porphyrin monomer (**P1**) indicating the orientations of the ZFS tensor and the hyperfine and nuclear quadrupole interaction tensors predicted for the nitrogen nuclei by DFT calculations with B3LYP/EPRII. The nitrogen hyperfine tensor ellipsoids are also depicted on the right. The Euler angles defining the orientation of the hyperfine tensors with respect to the ZFS tensor are α=19°, β=9° and γ=−145°, while the orientation of the nuclear quadrupole tensors are defined by α=81°, β=91° and γ=135° (angles for one ^{14}N nucleus, the other ones are related by symmetry).

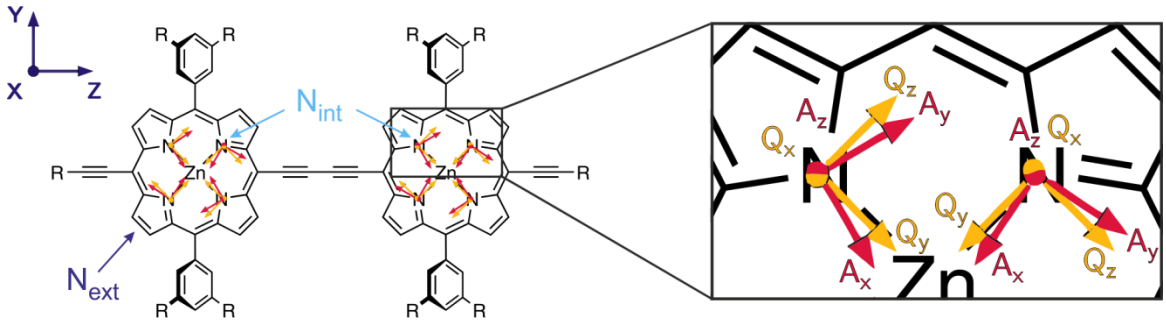

Figure S5. Diagram of the porphyrin dimer (**P2**) indicating the orientations of the ZFS tensor and the hyperfine and nuclear quadrupole interaction tensors predicted for the nitrogen nuclei by DFT calculations with B3LYP/EPRII. The Euler angles defining the orientation of the hyperfine tensors with respect to the ZFS tensor are α=33°, β=91° and γ=180° and α=30°, β=92° and γ=180°, while the orientation of the nuclear quadrupole tensors are defined by α=93°, β=45° and γ=90° for both internal and external nitrogen nuclei (angles for one ^{14}N nucleus of each type, the other ones are related by symmetry).

^{14}N ESEEM, ENDOR and HYSCORE simulations

Table S1. ^{14}N Hyperfine and Nuclear Quadrupole Interaction Parameters for P1 and P2.

		Opt	A_x [MHz]	A_y [MHz]	A_z [MHz]	Q [MHz]	η
P1	N	01	1.8±0.3	2.1±0.3	6.8±2.8	2.30±0.01	0.79±0.18
	N	02	0.4±0.3	0.6±0.3	6.8±2.8	2.30±0.01	0.79±0.18
P2	N_{ext}	01	0.8±0.2	1.1±0.2	3.5±1.4	2.25±0.01	0.75±0.20
	N_{int}	01	0.5±0.2	0.6±0.2	1.9±1.4	2.35±0.01	0.80±0.20
	N_{ext}	02	−0.6±0.2	−0.2±0.2	3.4±1.4	2.30±0.01	0.70±0.20
	N_{int}	02	−0.6±0.2	0.4±0.2	1.8±1.4	2.20±0.01	0.80±0.20

The hyperfine and nuclear quadrupole couplings were determined by fitting of the experimental data as described in the experimental section. The two sets of values correspond to an optimization assuming that the double-quantum features in the HYSCORE spectra of the X and Y orientations are due to both porphyrin and pyridine nitrogen nuclei (01) and assuming that they are only determined by pyridine nitrogen nuclei (02). The tensor orientations used in the simulations are derived from DFT calculations. The standard deviations indicate the distribution of values used in the simulations, there is an additional error on the center of the distribution of about 0.3 MHz for A_x and A_y, of 0.1 MHz for A_z, of 0.05 MHz for Q and of 0.1 on η.

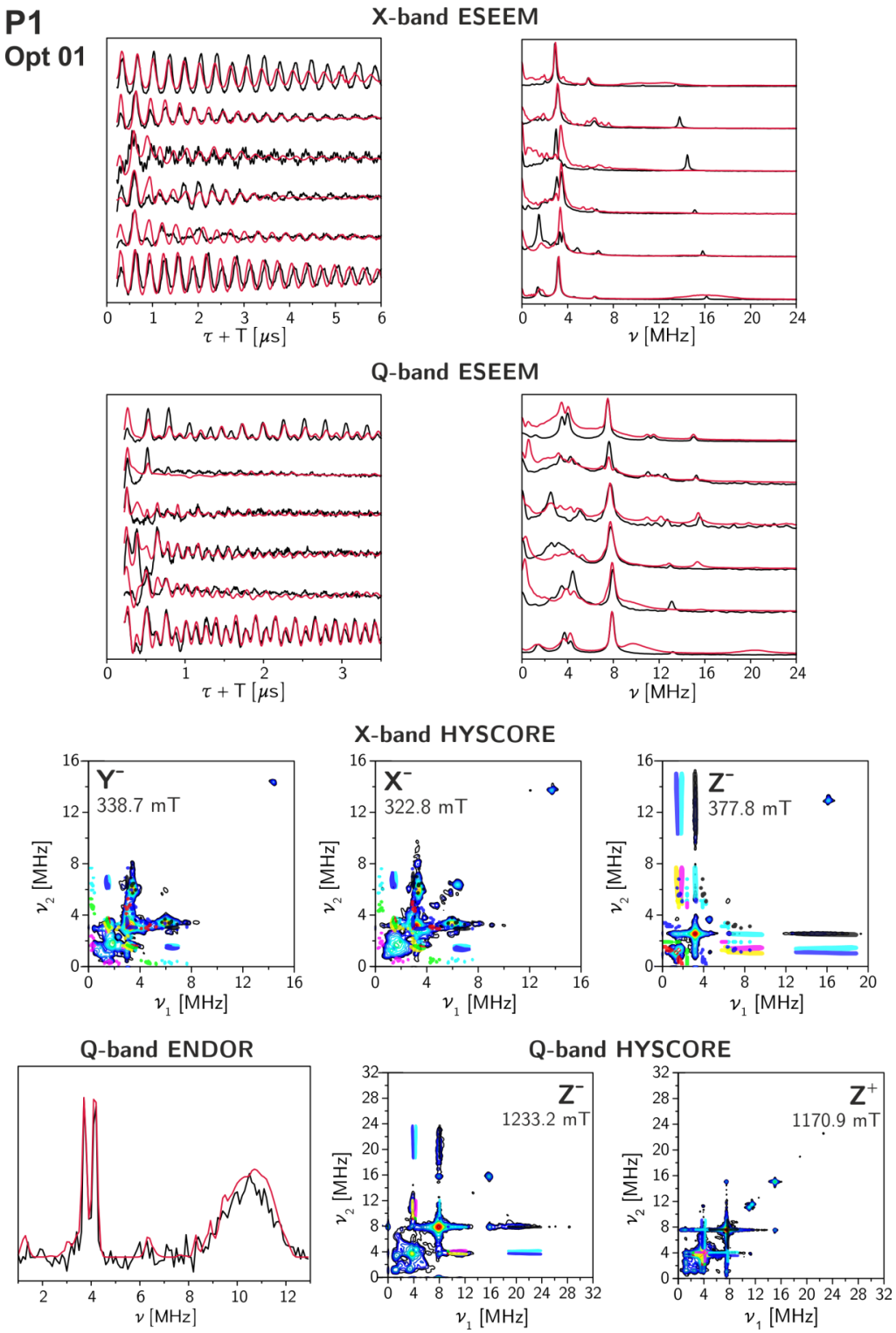

Figure S6. Experimental and simulated **P1** ^{14}N ESEEM and ENDOR data and calculated HYSCORE cross-peak positions for the first set of optimized parameters of SI table 1 (01, optimization assuming that both porphyrin and pyridine nitrogens contribute to the strongest cross-peaks in the HYSCORE spectra of the X and Y positions). All simulations except the time-domain ESEEM simulations include the contribution of pyridine nitrogens based on DFT calculations for a distribution of different pyridine-zinc distances. The calculated HYSCORE cross-peaks are color-coded based on the type of transitions: (ν_{dq}, ν_{dq}) - black, (ν_{dq}, ν_{sq}) - blue/cyan, (ν_{sq}, ν_{sq}) - green/magenta/yellow/red.

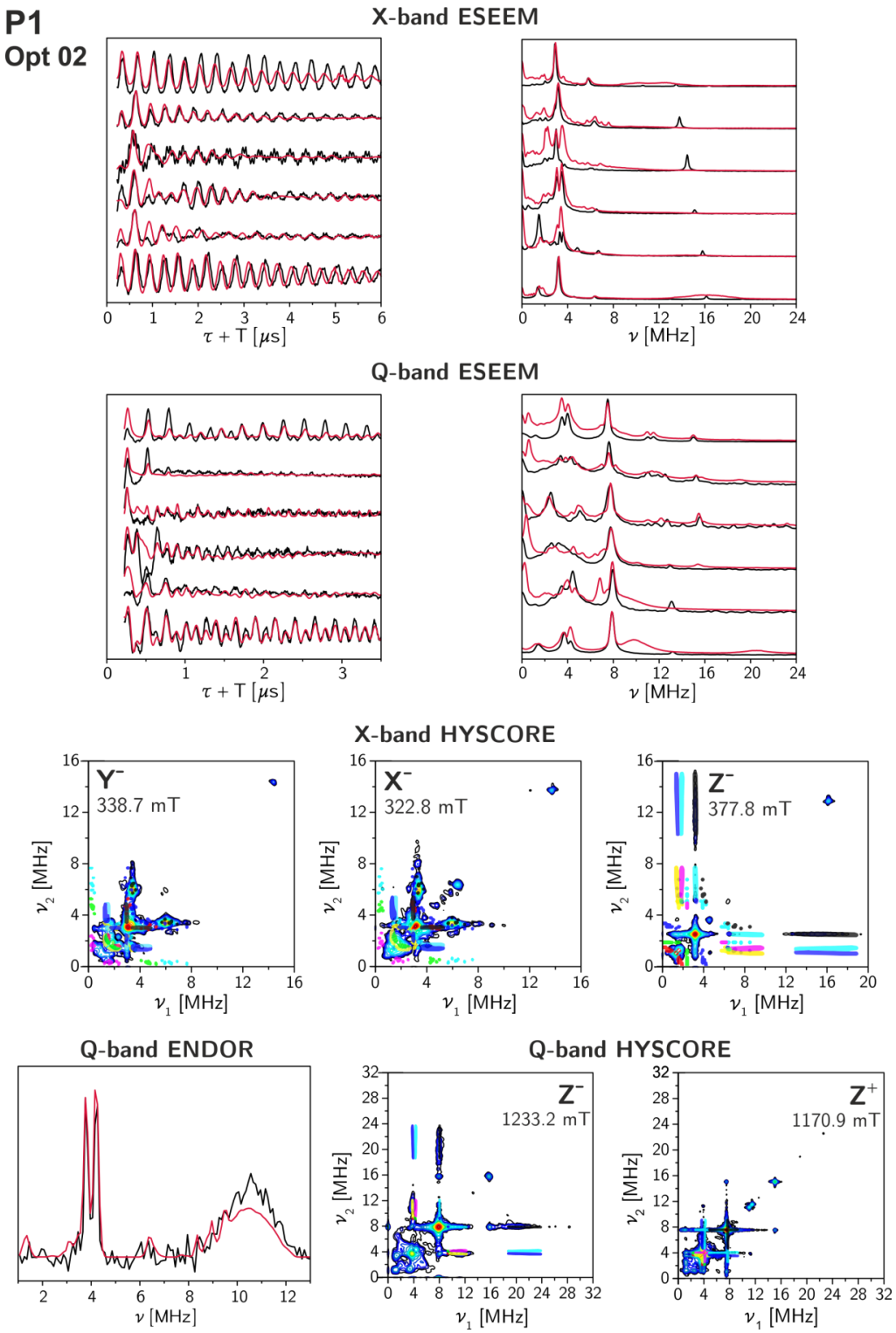

Figure S7. Experimental and simulated **P1** ^{14}N ESEEM and ENDOR data and calculated HYSCORE cross-peak positions for the first set of optimized parameters of SI table 1 (02, optimization assuming that only the pyridine nitrogens contribute to the strongest cross-peaks in the HYSCORE spectra of the X and Y positions). All simulations except the time-domain ESEEM simulations include the contribution of pyridine nitrogens based on DFT calculations for a distribution of different pyridine-zinc distances. The calculated HYSCORE cross-peaks are color-coded based on the type of transitions: (ν_{dq}, ν_{dq}) - black, (ν_{dq}, ν_{sq}) - blue/cyan, (ν_{sq}, ν_{sq}) - green/magenta/yellow/red.

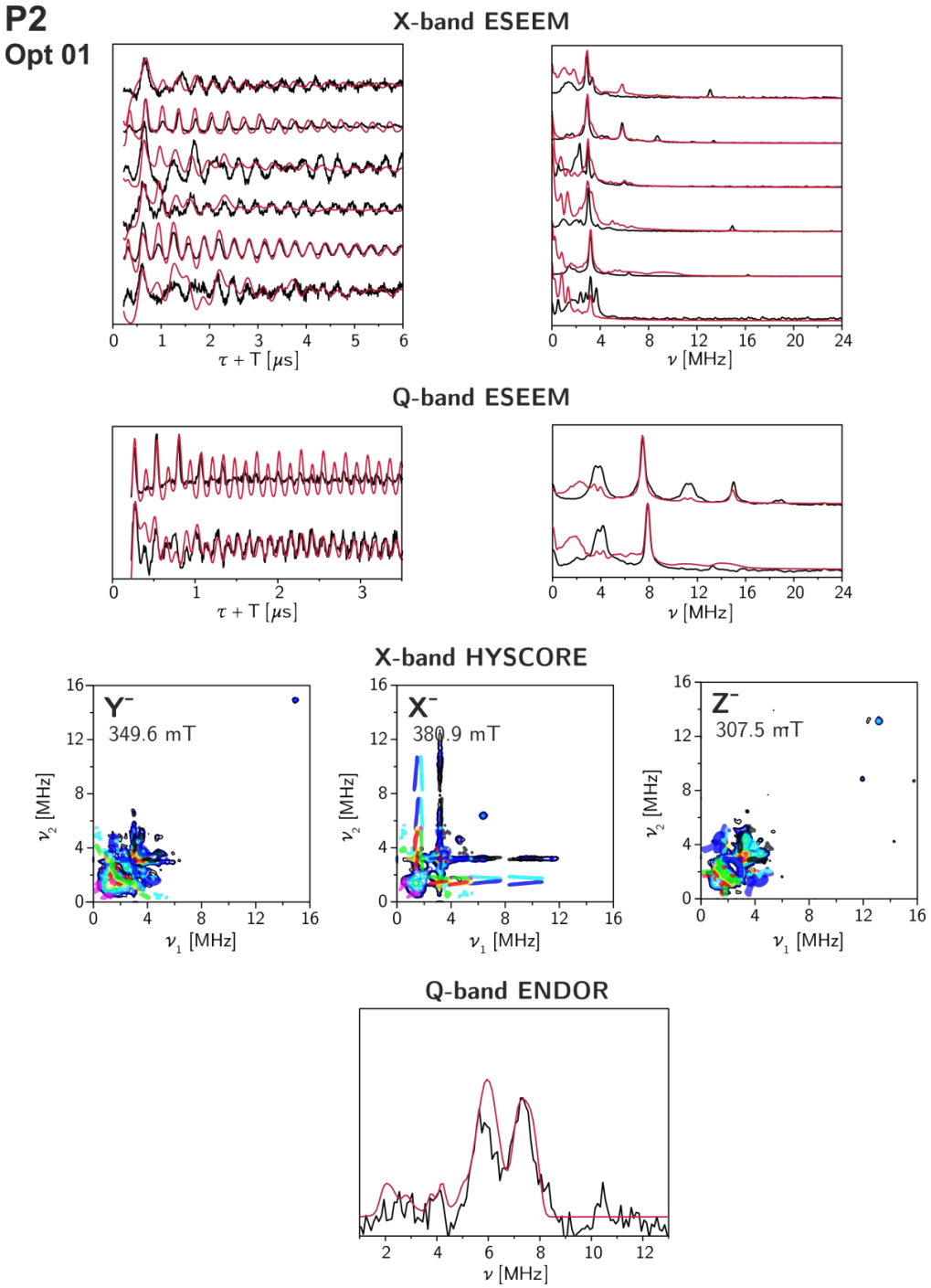

Figure S8. Experimental and simulated **P2** ^{14}N ESEEM and ENDOR data and calculated HYSCORE cross-peak positions for the first set of optimized parameters of SI table 1 (01, optimization assuming that both porphyrin and pyridine nitrogens contribute to the strongest cross-peaks in the HYSCORE spectra of the X and Y positions). All simulations except the time-domain ESEEM simulations include the contribution of pyridine nitrogens based on DFT calculations for a distribution of different pyridine-zinc distances. The calculated HYSCORE cross-peaks are color-coded based on the type of transitions: (ν_{dq}, ν_{dq}) - black, (ν_{dq}, ν_{sq}) - blue/cyan, (ν_{sq}, ν_{sq}) - green/magenta/yellow/red.

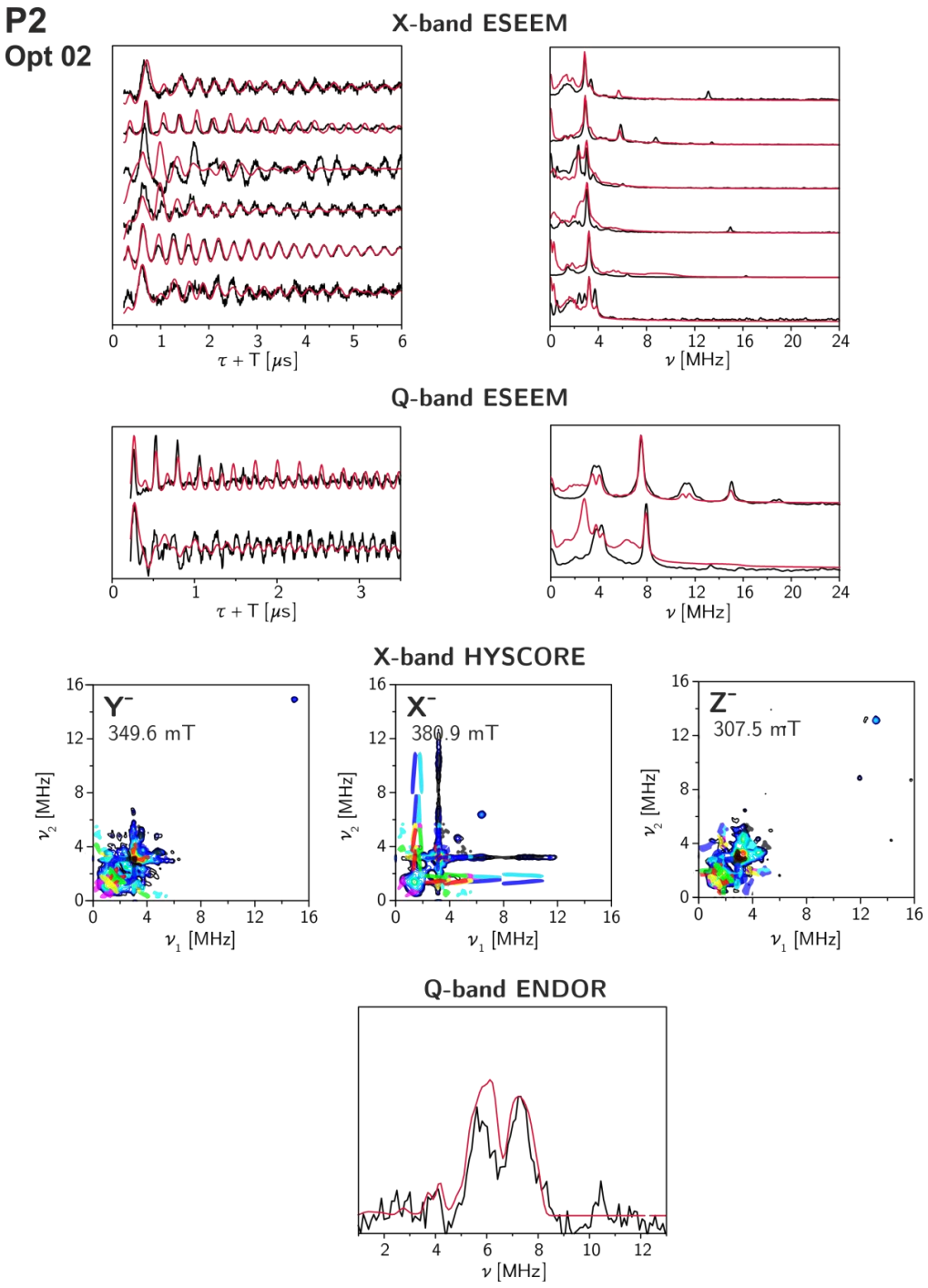

Figure S9. Experimental and simulated **P2** ^{14}N ESEEM and ENDOR data and calculated HYSCORE cross-peak positions for the first set of optimized parameters of SI table 1 (02, optimization assuming that only the pyridine nitrogens contribute to the strongest cross-peaks in the HYSCORE spectra of the X and Y positions). All simulations except the time-domain ESEEM simulations include the contribution of pyridine nitrogens based on DFT calculations for a distribution of different pyridine-zinc distances. The calculated HYSCORE cross-peaks are color-coded based on the type of transitions: (ν_{dq}, ν_{dq}) - black, (ν_{dq}, ν_{sq}) - blue/cyan, (ν_{sq}, ν_{sq}) - green/magenta/yellow/red.

References

1. Grozema, F. C.; Houarner-Rassin, C.; Prins, P.; Siebbeles, L. D. A.; Anderson, H. L. *J. Am. Chem. Soc.* **2007**, *129*, 13370-13371.
2. Van Doorslaer, S.; Sierra, G. A.; Schweiger, A. *J. Magn. Reson.* **1999**, *136*, 152-158.
3. Stoll, S.; Schweiger, A. *J. Magn. Reson.* **2006**, *178*, 42-55.
4. Siegel, S.; Judeikis, H. S. *J. Phys. Chem.* **1966**, *70*, 2205-2211.
5. Thurnauer, M. C.; Norris, J. R. *Chem. Phys. Lett.* **1977**, *47*, 100-105.
6. Stoll, S.; Britt, R. D. *Phys. Chem. Chem. Phys.* **2009**, *11*, 6614-6625.
7. Singel, D. J.; van der Poel, W. A. J. A.; Schmidt, J.; van der Waals, J. H.; De Beer, R. *J. Chem. Phys.* **1984**, *81*, 5453-5461.
8. Neese, F. *ORCA - an ab initio, Density Functional and Semiempirical program package*, 2.9/3.0; 2011.
9. Neese, F. *Wiley Interdiscp. Rev.: Comput. Mol. Sci.* **2012**, *2*, 73-78.
10. Sinnecker, S.; Neese, F. *J. Phys. Chem. A* **2006**, *110*, 12267-12275.
11. Barone, V., In *Recent Advances in Density Functional Methods, Part I*, Chong, D. P., Ed. World Scientific Publ. Co.: Singapore, 1996.
12. Weigend, F.; Ahlrichs, R. *Phys. Chem. Chem. Phys.* **2005**, *7*, 3297-3305.
13. Petrenko, T.; Kossmann, S.; Neese, F. *J. Chem. Phys.* **2011**, *134*, 054116.
14. Barone, V. *J. Chem. Phys.* **1994**, *101*, 6834-6838.
15. Barone, V. *J. Chem. Phys.* **1994**, *101*, 10666-10676.
16. Winters, M. U.; Kärnbratt, J.; Eng, M.; Wilson, C. J.; Anderson, H. L.; Albinsson, B. *J. Phys. Chem. C* **2007**, *111*, 7192-7199.
17. Peeks, M. D.; Neuhaus, P.; Anderson, H. L. *manuscript in preparation*.